Treatment of laser-induced thermal acoustics in the framework of discrete kinetic theory

F. Hanser,* W. Koller,† and F. Schürrer‡
Institute for Theoretical Physics, Technical University Graz, Petersgasse 16, A-8010 Graz, Austria
(Received 24 May 1999; revised manuscript received 3 September 1999)

The physics behind the laser-induced thermal acoustics technique is dealt with on a microscopic level. A discrete velocity model of the Boltzmann equation for inelastically interacting gas mixtures in the presence of two counterpropagating laser beams is established. The collisional scheme for the model is developed by taking into account elastic and inelastic interactions between the gas particles, on the one hand, and the interactions between monochromatic laser photons and gas particles, on the other hand. The formation and evolution of laser-pulse-driven thermal and density gratings are simulated by numerically solving the discrete kinetic equations based on the fractional step method. Numerical results are provided for a wide scope of Knudsen numbers.

PACS number(s): 02.70.−c, 51.10.+y, 47.45.−n, 33.50.Hv

I. INTRODUCTION

The excitation of acoustic and thermal waves by the use of pulsed laser light is a well-known phenomenon. It was first reported as an artifact in degenerate four-wave-mixing experiments performed on strongly absorbing transitions in collision-dominated gas-phase systems [1].

A recently presented method based on this phenomenon is the laser-induced thermal acoustics (LITA). It is an optical four-wave-mixing (FWM) technique for remotely and nonintrusively measuring the physical and chemical properties of gases. The development of this technique by Cummings [2] addressed issues including the need to make measurements in a single laser pulse as well as the need to make measurements in extremely challenging environments. Some examples are measurements in the primary and reflected-shock regions at the exit of a combustion driven shock tube or measurements of low concentrations of toxic gases in combustion engines [3].

LITA scattering is subdivided into two steps. In the first step, light from a powerful pulsed laser is split into two phase-coherent beams that intersect at a shallow angle. The region of the intersection of the two laser beams defines the sample volume. The interference of the driver laser beams creates an electric field intensity grating. The gas mixture in the sample volume responds to the intensity grating by optoacoustic effects. The two major optoacoustic effects are thermalization and electrostriction. These effects can perturb the bulk properties of the medium. Other optoacoustic effects, including photophoresis and thermophoresis, are of minor importance.

The second step involves scattering of a source beam laser into a coherent signal beam by optoacoustic effects. In gases, the most important effect is scattering from density perturbations. The signal beam is modulated in time by the evolution of laser-induced perturbations. From these modulations, accurate physical properties of the medium may be inferred, including the sound speed, thermal diffusivity, and other properties that affect the development of the laser-induced gratings. Therefore, deep insight and understanding of the dominant processes is very important.

On physical grounds, the formation and evolution of these gratings has been treated using the equations of fluid dynamics in its linearized form [4]. This assumes a uniform behavior of the medium and small perturbations. In addition, the assumption of linear hydrodynamic behavior eliminates a variety of phenomena which could affect the signals in real experiments. Moreover, using hydrodynamic equations assumes scales of gradients of fluid properties to be small compared to molecular mean-free paths. This implies that for large Knudsen numbers (a ratio between a laboratory length and the mean free path) or in situations in which nonlinear effects gain importance, other models have to be used.

Cummings himself proposed resorting to a molecular gas-dynamics model. A microscopic approach also allows the investigation of the evolution of each component of the medium. This could be interesting when one deals with species gratings which are generally ignored. A model describing the medium on a microscopic level consists of a set of Boltzmann equations for inelastically interacting gas mixtures [5–7]. These coupled nonlinear integrodifferential equations oppose direct analytical and numerical treatment [5,6]. One way out of this problem is the discretization of the velocity space [8,9]. Early discrete velocity models of the continuous Boltzmann equation refer to idealized gases with only one or two particle speeds [10–12]. This was a big shortcoming because the temperature was ill defined, and it would be an exaggeration to speak of a velocity distribution when only two velocity moduli were involved. The physical discrete models, however, are the multispeed ones [13].

In this paper a discrete velocity model of Shizuta type with six speeds is used to describe the formation and dynamics of laser-induced density and thermal gratings. Section II deals with the general microscopic model. We describe the physical situation together with the dominant interaction processes. We introduce the discrete velocity model and discuss its most relevant features. From the discrete velocity model we derive the discrete kinetic equations which govern the system. The last subsection treats some aspects of equilib-

*Electronic address: hanser@itp.tu-graz.ac.at
†Electronic address: kowin@itp.tu-graz.ac.at
‡Electronic address: schuerrer@itp.tu-graz.ac.at

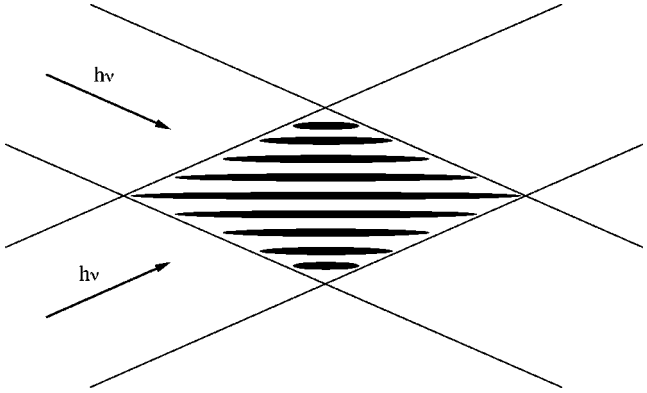

FIG. 1. Experimental situation: The region of the intersection of the two driver laser beams defines the sample volume.

rium. In Sec. III we solve numerically the discrete kinetic equations by applying the fractional step method. We simulate the formation and evolution of the laser-induced gratings in different situations. Finally, in Sec. IV we give a conclusion.

II. MICROSCOPIC MODEL

A. Physical situation

As already mentioned in Sec. I, and as can be seen in Fig. 1, the region of intersection of the two driver laser beams defines the sample volume. The two driver beams interfere forming an intensity grating. In our formalism the laser intensity is represented by photons p. The gas mixture in the sample volume is composed of the molecules A, their electronically excited state A^*, and a second species B with masses m_A, m_{A^*} and m_B, respectively. The laser frequency ν is tuned to excite the electronic transition between the molecules A and A^*. The energy gap of the transition is given by $\Delta E = E(A^*) - E(A) = h\nu$. On a microscopic level, the molecules are allowed to undergo the following types of interaction processes: (1) elastic scattering between the molecules,

$$M + N \rightleftharpoons M + N \quad \text{for } M,N = A,A^*,B;$$

(2) collisional excitation of molecules A,

$$A + A \rightarrow A^* + A,$$

$$A + B \rightarrow A^* + B;$$

(3) collisional de-excitation of molecules A^*,

$$A^* + A \rightarrow A + A,$$

$$A^* + B \rightarrow A + B;$$

(4) spontaneous emission of photons p by molecules A^*,

$$A^* \rightarrow A + p;$$

(5) absorption of photons p by molecules A,

$$A + p \rightarrow A^*;$$

and (6) stimulated emission of photons p by molecules A^*,

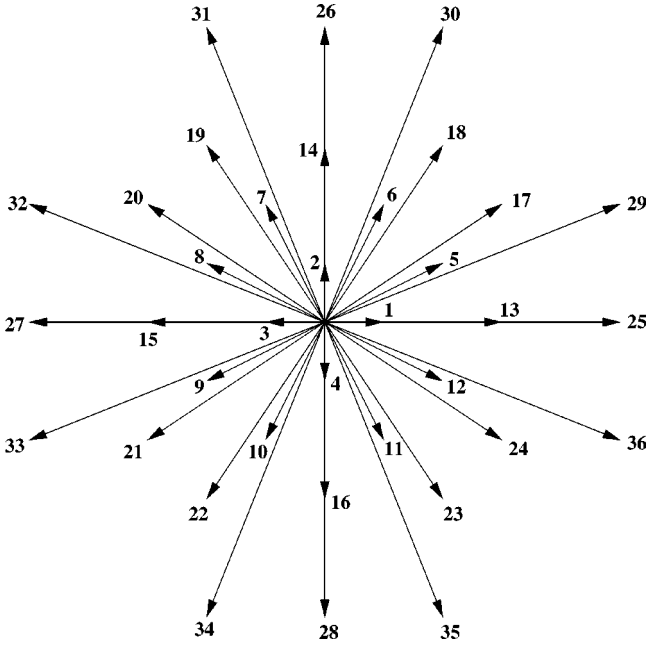

FIG. 2. Regular discrete velocity model of Shizuta type with 36 velocities and six speeds.

$$A^* + p \rightarrow A + p + p.$$

The elastic particle-particle scattering processes are modeled by elastic hard sphere cross sections $\sigma^{el}_{MN\rightarrow MN}$, with $M,N = A,A^*,B$, whereas the collisional excitation processes are indicated by the cross sections $\sigma^{in}_{AA\rightarrow AA^*}$ and $\sigma^{in}_{AB\rightarrow A^*B}$. The inelastic cross sections $\sigma^{in}_{AA^*\rightarrow AA}$ and $\sigma^{in}_{A^*B\rightarrow AB}$ for the inverse processes (collisional de-excitation) are determined by a microreversibility condition [7].

Interactions between photons p of the pulsed driver laser and particle species A and A^* are taken into account by means of the Einstein coefficients α and β [14]. Spontaneous emission of photons is controlled by α. The magnitude of absorption and stimulated emission phenomena is proportional to β.

B. Discrete velocity model

The idealized physical situation sketched above in Sec. II A is essentially one-dimensional in real space. However, when treating four-wave mixing in a two-dimensional phase space on a kinetic level, energy and momentum conservation rule out all nontrivial collisions. Therefore, we have to choose at least a two-dimensional discrete velocity model (DVM).

Figure 2 shows a Shizuta type DVM [9] with 36 velocities and six speeds of relative magnitude a, $\sqrt{5}a$, $3a$, $\sqrt{13}a$, $5a$, $\sqrt{29}a$. Later on the DVM scaling parameter a is adapted to fit the physical situation.

For good relaxational behavior, multiple speed collisions by which we denote binary collisions with three and four different speeds are crucial. Therefore, the chosen model is of Shizuta type, allowing elastic multiple speed collisions between all species, as, for instance

$$(\mathbf{v}_4,\mathbf{v}_{22}) \rightleftharpoons (\mathbf{v}_9,\mathbf{v}_{16}), \quad (\mathbf{v}_1,\mathbf{v}_{21}) \rightleftharpoons (\mathbf{v}_8,\mathbf{v}_{16}),$$

$$(\mathbf{v}_3,\mathbf{v}_{29}) \leftrightharpoons (\mathbf{v}_7,\mathbf{v}_{25}), \quad (\mathbf{v}_{13},\mathbf{v}_{32}) \leftrightharpoons (\mathbf{v}_{17},\mathbf{v}_{27}).$$

It should be noted that at least 50% of all binary collisions involve more than two speeds.

Moreover, in the case of four-wave mixing, inelastic collisions represent collisional excitation and de-excitation processes. Thus the model must provide such interactions for an appropriately fixed energy gap q. Shizuta type models meet this requirement for several possible values of q. For the energy gap $q=12m_Aa^2$ (we assume $m_A=m_{A*}$) exemplary collisions involving four different speeds are given by

$$(\mathbf{v}_5,\mathbf{v}_{33}) \leftrightharpoons (\mathbf{v}_4,\mathbf{v}_{15})+q,$$

$$(\mathbf{v}_{10},\mathbf{v}_{29}) \leftrightharpoons (\mathbf{v}_1,\mathbf{v}_{13})+q,$$

$$(\mathbf{v}_{13},\mathbf{v}_{32}) \leftrightharpoons (\mathbf{v}_1,\mathbf{v}_{20})+q.$$

The above considerations imply that the collisional scheme shows all features necessary to meet the requirements of a kinetic description of four-wave mixing.

It is clear that establishing a DVM consisting of a rather high number of velocities and three distinguishable species demands sophisticated computational techniques. The major problem to overcome is the high number (about 10^4) of admissible collisions inflating the collisional term of the kinetic equations. A computer program especially developed and tested by one of the authors (F.H.) yields the complete collisional scheme. The input data of this program are the velocity vectors, the number of species, the masses of each species, and the types of interactions taken into account.

C. Discrete Boltzmann equations

The governing equations for the number densities of all three species of the gas mixture are a set of coupled nonlinear Boltzmann equations. Equipped with the complete collisional scheme of the system, we can formulate the equations

$$\left(\frac{\partial}{\partial t}+\mathbf{v}_i^A\cdot\frac{\partial}{\partial \mathbf{x}}\right)N_i^A=\mathcal{J}_i^A[\underline{N}^M]+\mathcal{R}_i^A[\underline{N}^M,I], \tag{1a}$$

$$\left(\frac{\partial}{\partial t}+\mathbf{v}_i^{A*}\cdot\frac{\partial}{\partial \mathbf{x}}\right)N_i^{A*}=\mathcal{J}_i^{A*}[\underline{N}^M]-\mathcal{R}_i^A[\underline{N}^M,I], \tag{1b}$$

$$\left(\frac{\partial}{\partial t}+\mathbf{v}_i^B\cdot\frac{\partial}{\partial \mathbf{x}}\right)N_i^B=\mathcal{J}_i^B[\underline{N}^M], \tag{1c}$$

where $N_i^M(\mathbf{x},t)$ is the number density of the molecules M $(M=A,A^*,B)$ with velocity $\mathbf{v}_i^M$ $(i=1,\ldots,36)$ at the point $\mathbf{x}$ at time t and $\underline{N}^M$ is an abbreviation of $(N_1^M,\ldots,N_{36}^M)$.

The right hand sides of Eqs. (1) are the collision terms due to the interaction processes described in Sec. II A. Interactions between the radiation intensity and the particle species A and A^* are taken into account by

$$\mathcal{R}_i^A[\underline{N}^M,I]=(\alpha+\beta I)N_i^{A*}-\beta I N_i^A,$$

where $I=I(\mathbf{x},t)$ is the laser intensity. The functionals $\mathcal{J}_i^A[\underline{N}^M]$, $\mathcal{J}_i^{A*}[\underline{N}^M]$, and $\mathcal{J}_i^B[\underline{N}^M]$ are the collision terms concerning interactions between the particles. Each particle-particle collision event (elastic scattering, collisional excitation and deexcitation) generates an expression of quadratic nonlinearity in the number densities of the molecules. The particular form reads

$$A_{i,j}^{k,l}(N_k^{M'}N_l^{N'}-N_i^MN_j^N),$$

with $M',N',M,N=A,A^*,B$. The transition rates $A_{i,j}^{k,l}$ are defined in the following way:

$$A_{i,j}^{k,l}=\sigma_{MN\to M'N'}^{el(in)}(|\mathbf{v}_i^M-\mathbf{v}_j^N|)|\mathbf{v}_i^M-\mathbf{v}_j^N|a_{i,j}^{k,l}.$$

The transition probability of each particle-particle event is taken into account by $a_{i,j}^{k,l}$. For more detailed information about symmetry relations of $A_{i,j}^{k,l}$, see Ref. [9]. The complete expressions of the collision terms are very cumbersome, and are therefore not quoted here. Their actual expressions can be obtained from the authors.

The macroscopic quantities of interest are the number densities of each species n^M, the total number density n, the mass density of each species ρ^M, the mass density of the whole mixture ρ, the average gas velocity of each species $\mathbf{u}^M$, the average gas velocity of the whole mixture $\mathbf{u}$, the average internal kinetic energy of each species e^M, and the average internal kinetic energy of the whole mixture e. The species related macroscopic quantities are defined in the usual way:

$$n^M=\sum_{i=1}^{36}N_i^M \quad \text{for} \quad M=A,A^*,B, \tag{2a}$$

$$\rho^M=m^Mn^M \quad \text{for} \quad M=A,A^*,B, \tag{2b}$$

$$\mathbf{u}^M=\frac{1}{\rho^M}\sum_{i=1}^{36}m^M\mathbf{v}_i^MN_i^M, \tag{2c}$$

$$e^M=\frac{1}{n^M}\sum_{i=1}^{36}\frac{1}{2}m^M(\mathbf{v}_i^M-\mathbf{u}^M)^2N_i^M. \tag{2d}$$

The quantities for the whole gas mixture are defined as follows:

$$n=\sum_M n^M, \tag{3a}$$

$$\rho=\sum_M \rho^M, \tag{3b}$$

$$\mathbf{u}=\frac{1}{\rho}\sum_M\sum_{i=1}^{36}m^M\mathbf{v}_i^MN_i^M, \tag{3c}$$

$$e=\frac{1}{n}\sum_M\sum_{i=1}^{36}\frac{1}{2}m^M(\mathbf{v}_i^M-\mathbf{u})^2N_i^M. \tag{3d}$$

It should be noted that all macroscopic quantities in Eqs. (2) and (3) are functions of space $\mathbf{x}$ and time t.

D. Equilibrium conditions

The state of the whole gas mixture in the sample volume before the powerful driver laser pulse starts interacting with the gas species A and A^* is assumed to be a thermodynamical equilibrium state. Therefore, it is necessary to specify conditions at equilibrium. In our model, equilibrium is established if all particle-particle collision terms of Eqs. (1) simultaneously vanish [5]. This means

$$\mathcal{J}_i^A[\underline{N}^A,\underline{N}^{A^*},\underline{N}^B]=0, \tag{4a}$$

$$\mathcal{J}_i^{A^*}[\underline{N}^A,\underline{N}^{A^*},\underline{N}^B]=0, \tag{4b}$$

$$\mathcal{J}_i^B[\underline{N}^A,\underline{N}^{A^*},\underline{N}^B]=0. \tag{4c}$$

Equilibrium concerning the elastic particle-particle scattering processes is fulfilled by the following expressions for the number densities:

$$N_i^M=\alpha^M\exp[\mathbf{c}\cdot\mathbf{v}_i^M-\beta|\mathbf{v}_i^M|^2], \tag{5}$$

where α^M, $\mathbf{c}$, and β are the so-called Maxwellian parameters. In addition, demanding equilibrium concerning the collisional excitation and de-excitation processes yields the condition

$$\alpha^{A^*}=\alpha^A\exp[-\beta q], \tag{6}$$

where the quantity q is the difference of the precollisional and postcollisional kinetic energies. Since the laser frequency is assumed to be tuned to excite the electronic transition of species A and A^*, the internal energy q is equal to $h\nu$. The Doppler effect, though essential for a variety of photon-gas interactions such as laser cooling [15], is of no importance in FWM, and is therefore neglected by our model.

The resulting independent Maxwellian parameters α^A, α^B, $\mathbf{c}$, and β are related by a one-to-one map to the independent macroscopic quantities of the system [9]. As a particular result it can easily be shown that $\mathbf{c}=\mathbf{0}$ implies $\mathbf{u}^M=\mathbf{u}=\mathbf{0}$, and vice versa. However, it is not possible, in general, to express the Maxwellian parameters as functions of the independent macroscopic quantities in terms of analytic functions. Despite this shortcoming, we are able to fix a thermodynamical equilibrium state by simply specifying the independent Maxwellian parameters.

III. SIMULATIONS

In this section we investigate the formation and evolution of the driver laser-induced thermal and density gratings. Several different cases are studied. To this end, we solve numerically the set of coupled discrete Boltzmann equations, i.e., Eqs. (1), for suitable initial and boundary conditions. Since the period of the intensity grating formed by the two driver laser beams (e.g., the fringe spacing λ) is very small compared with the extension of the sample volume, we assume both the extension of the intensity grating and the sample volume to be infinite. Based on this assumption, it is sufficient to consider only one fringe spacing together with periodic boundary conditions. The fringe spacing depends on the laser frequency and the angle of intersection of the laser beams [4]. Typical values range from 1 to 30 μm. For our simulations we fix this value to $\lambda=6$ μm.

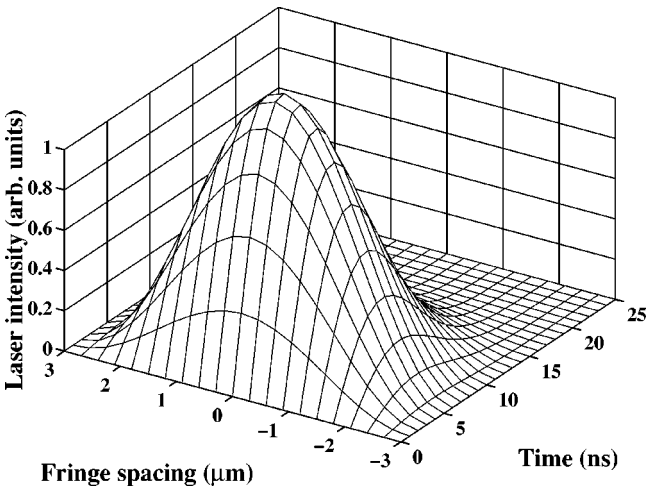

FIG. 3. Temporal and spatial intensity profile of the pulsed driver laser.

The DVM scaling parameter a is determined by resorting to the fact that a sufficiently small perturbation propagates with the speed of sound, which is around 330 ms^{-1} for a gas, say air, at standard conditions. A value of $a=500$ ms^{-1} fulfills this requirement and adjusts the underlying DVM to our physical situation.

For the number density of molecules B we choose $n^B=10^{25}$ m^{-3}, a value that is typical of standard conditions. Molecules A and A^* are considered to be of low concentration, and therefore we choose $n^A+n^{A*}=10^{-3}n^B$. Without loss of generality we fix the mass ratio $m^A/m^B=1$. This allows us to use only one DVM, which means that $\mathbf{v}_i^A=\mathbf{v}_i^{A*}=\mathbf{v}_i^B$. This is a good approximation for NO, NO*, and O_2.

The temporal and spatial profile of the intensity in the sample volume is described by the formula [4]

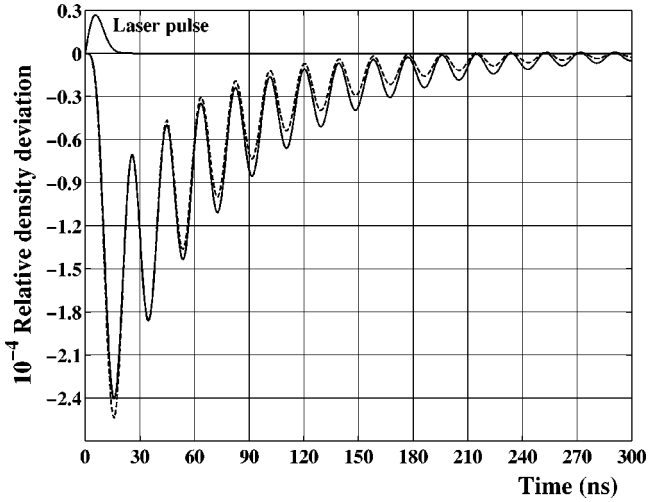

FIG. 4. Time evolution of the relative density deviation in the middle of the fringe spacing. The dashed and solid lines show the results obtained by the fluid dynamic and the discrete kinetic model (Kn=0.0033), respectively.

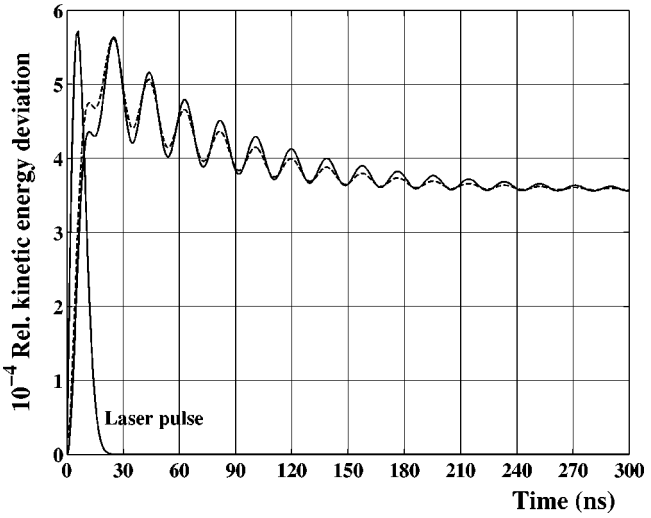

FIG. 5. Time evolution of the relative energy density deviation in the middle of the fringe spacing. The dashed and solid lines show the results obtained by the fluid dynamic and the discrete kinetic model (Kn=0.0033), respectively.

$$I(t,x)=I_0\frac{2t}{\tau^2}\exp\left[-\left(\frac{t}{\tau}\right)^2\right]\cos^2\left(\frac{\pi}{\lambda}x\right),$$

where $x\in[-\lambda,\lambda]$ and $t\in[0,\infty)$. A graphical representation is sketched in Fig. 3. The quantity τ indicates the duration of the laser pulse. We fix this parameter to $\tau=8$ ns. The strength of the laser intensity is controlled by I_0. A chosen value for the product $\beta I_0=10^9\ \mathrm{s}^{-1}$ causes the ratio n^{A*}/n^A to be approximately 10^{-2} (the weak pumping limit). The effect of spontaneous emission modeled by the Einstein coefficient α is for the formation and evolution of the gratings of minor importance. Nevertheless, we take this effect into account by assigning α the value $10^5\ \mathrm{s}^{-1}$.

On a microscopic level the different physical situations are characterized by the cross sections introduced in Sec. II A. To simulate these situations, we have to specify six elastic and two inelastic cross sections. To restrict the variety

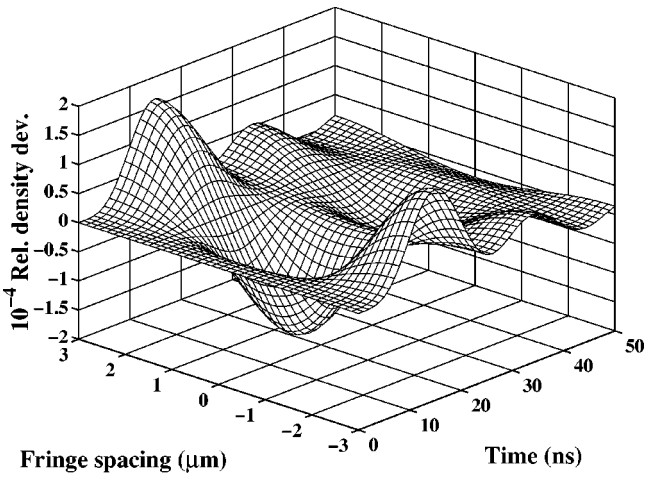

FIG. 6. Time-space evolution of the relative density deviation inside the fringe spacing for a Knudsen number Kn=0.0167 and an inelastic cross section $\sigma^{in}=1\ \mathrm{nm}^2$.

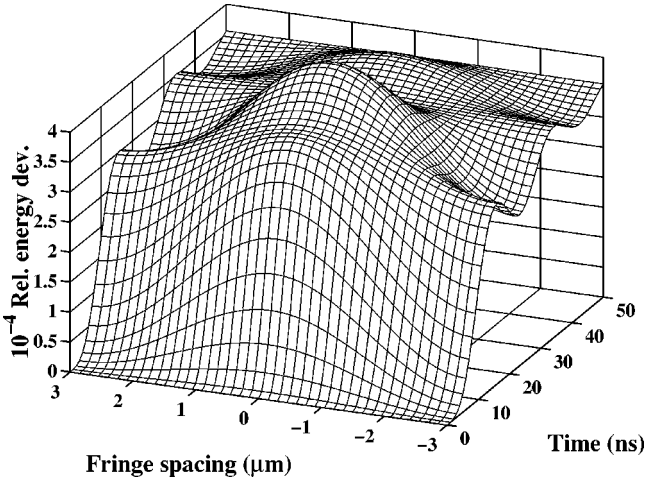

FIG. 7. Time-space evolution of the relative kinetic energy deviation inside the fringe spacing for a Knudsen number Kn=0.0167 and an inelastic cross section $\sigma^{in}=1\ \mathrm{nm}^2$.

of possible variations, we assume all elastic and the two inelastic cross sections to have the same value. This reads in detail as

$$\sigma^{el}=\sigma^{el}_{MN\to MN}\quad\text{for}\quad M,N=A,A^*,B$$

and

$$\sigma^{in}=\sigma^{in}_{AA\to AA^*}=\sigma^{in}_{AB\to A^*B}.$$

For a characterization of the dominant gas species B, we introduce a Knudsen number which is defined, as usual, in the following way:

$$\mathrm{Kn}=\frac{1}{\lambda\sigma^{el}n^B}.$$

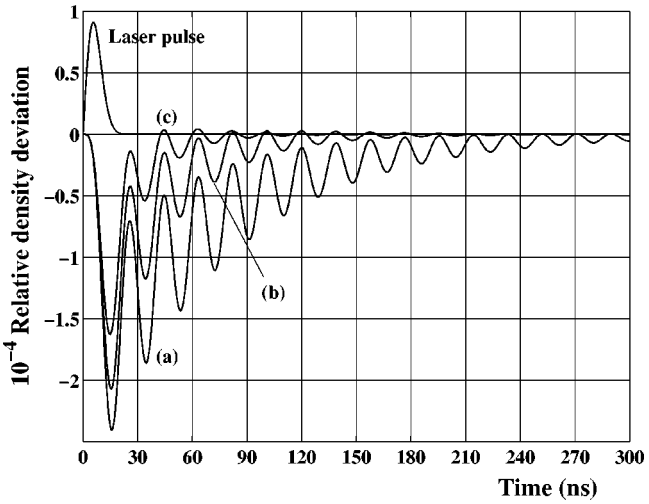

FIG. 8. Relative density deviation in the middle of the fringe spacing for an inelastic cross section $\sigma^{in}=1\ \mathrm{nm}^2$. (a), (b), and (c) correspond to Knudsen numbers Kn with values 0.0033, 0.0083, and 0.0167, respectively.

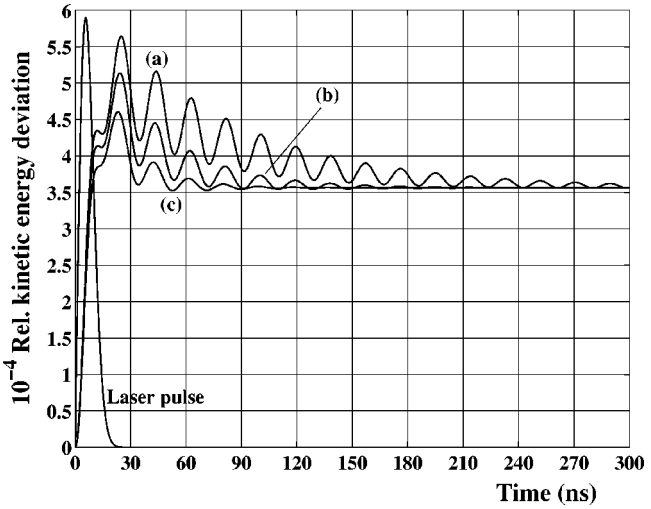

FIG. 9. Relative kinetic energy deviation in the middle of the fringe spacing for an inelastic cross section $\sigma^{in}=1$ nm^2. (a), (b), and (c) correspond to Knudsen numbers Kn with values 0.0033, 0.0083, and 0.0167, respectively.

Based on the fractional step method [16–18], we perform numerical simulations for a wide range of Knudsen numbers by simultaneously varying the inelastic cross sections.

The following subsections present the profiles of the relative density deviation

$$\frac{n^B(t,x)-n^B(0,x)}{n^B(0,x)}$$

and the relative kinetic energy deviation

$$\frac{e^B(t,x)-e^B(0,x)}{e^B(0,x)}.$$

The three-dimensional plots show the temporal and spatial evolution of these quantities for a selected inelastic cross section. The two-dimensional plots show the temporal evolution in the middle of the fringe spacing for several Knudsen numbers and inelastic cross sections.

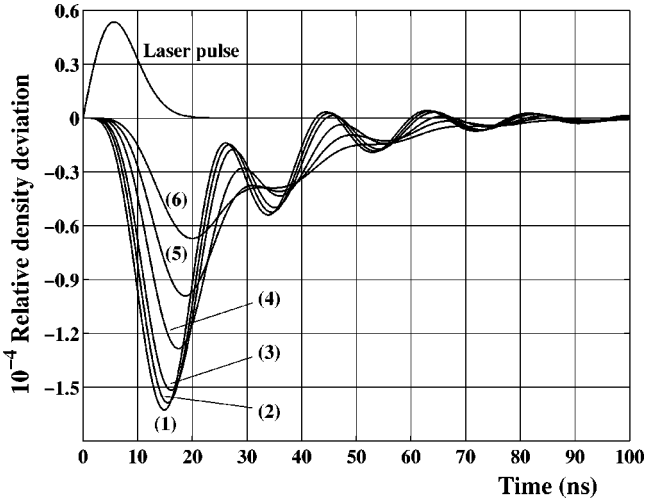

FIG. 10. Relative density deviation in the middle of the fringe spacing for a Knudsen number Kn=0.0167. Curves (1), (2), (3), (4), (5), and (6) correspond to inelastic cross sections σ^{in} with values 1, 0.1, 0.05, 0.02, 0.01, and 0.005 nm^2, respectively.

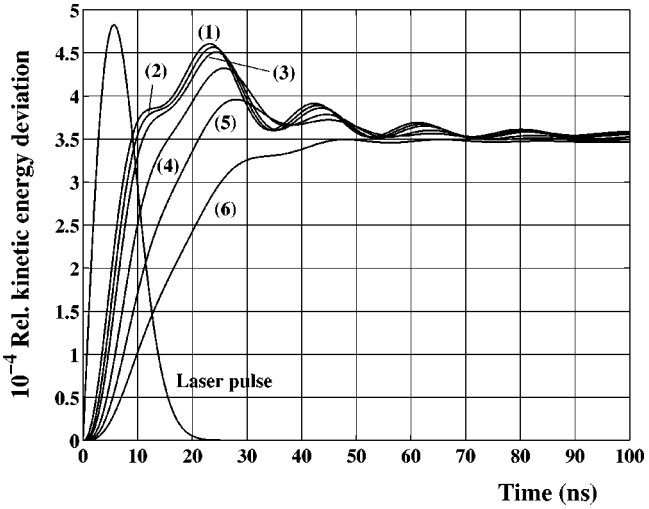

FIG. 11. Relative kinetic energy deviation in the middle of the fringe spacing for a Knudsen number Kn=0.0167. Curves (1), (2), (3), (4), (5), and (6) correspond to inelastic cross sections σ^{in} with values 1, 0.1, 0.05, 0.02, 0.01, and 0.005 nm^2, respectively.

A. Low Knudsen numbers

In this range of Knudsen numbers the gas mixture behaves as a fluid, and therefore the problem can also be treated in the framework of fluid dynamics. Moreover, since the perturbations are sufficiently small, linearized fluid dynamic equations have shown good agreement with experimental results [4].

This well-established approach provides a possibility to compare our discrete model with the Boltzmann equation at low Knudsen numbers. To this end, we solve the linearized equations of fluid dynamics for the dominant species [2], whereas the laser energy deposit is taken into account by a gain term on the right hand side of the energy equation [4]. The transport coefficients entering these equations, namely,

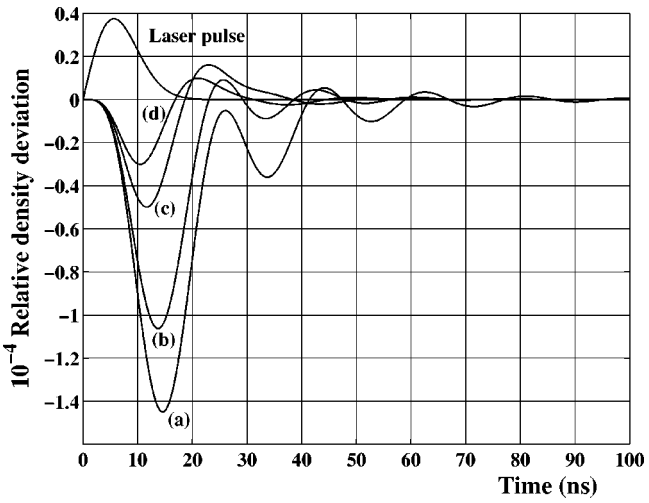

FIG. 12. Relative density deviation in the middle of the fringe spacing for an inelastic cross section $\sigma^{in}=1$ nm^2. (a), (b), (c), and (d) correspond to Knudsen numbers Kn with values 0.021, 0.033, 0.083, and 0.167, respectively.

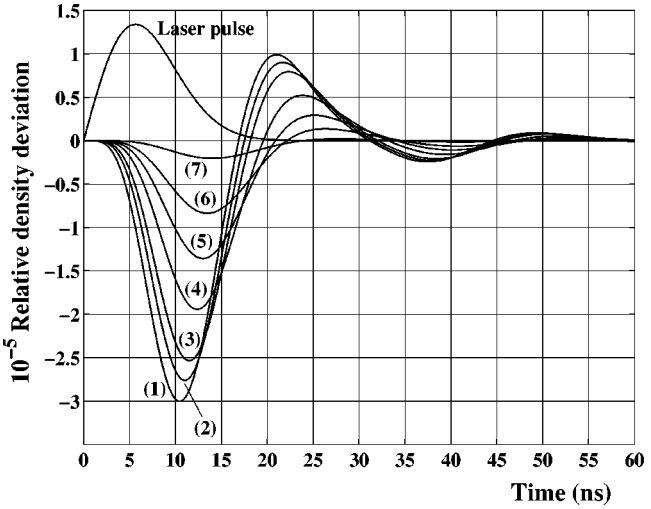

FIG. 13. Relative density deviation in the middle of the fringe spacing for a Knudsen number Kn=0.167. Curves (1), (2), (3), (4), (5), (6), and (7) correspond to inelastic cross sections σ^{in} with values 1, 0.1, 0.05, 0.02, 0.01, 0.005, and 0.001 nm^2, respectively.

the thermal conductivity and the kinematic viscosity, are obtained by the Chapman–Enskǿg perturbation technique [19] for monatomic hard sphere molecules. Figures 4 and 5 show a comparison between the fluid dynamic approach and the kinetic model, where we observe good agreement. In particular, the structures of the density and energy oscillations match. The small discrepancies between the two approaches are attributed to the discrete character of our kinetic model.

Furthermore, a faster energy deposit into the system is observed in the case of the fluid dynamic model. Here the deposition of the laser energy is described by a one step process. In the kinetic model, however, the physically more realistic two step process, namely, excitation of a rare species and deposit of kinetic energy by collisional deexcitation events, is taken into account. This explains the slower deposit of the laser energy in the latter case. Consequently, the simulations using our DVM give a valid picture of the physics of thermal gratings in the fluid dynamic limit.

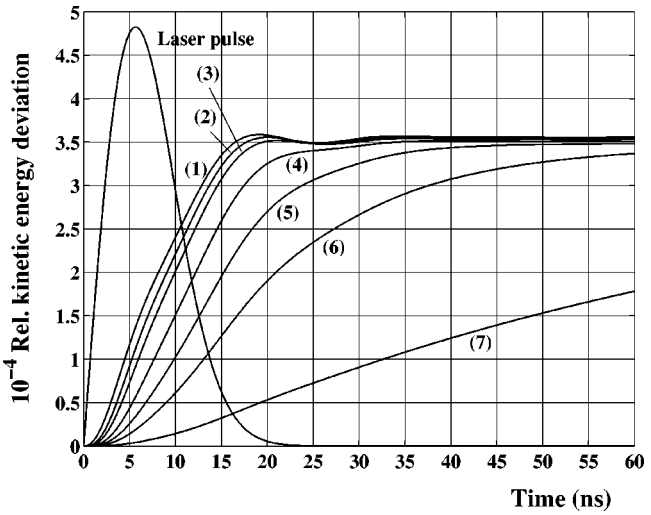

FIG. 14. Relative kinetic energy deviation in the middle of the fringe spacing for a Knudsen number Kn=0.167. Curves (1), (2), (3), (4), (5), (6), and (7) correspond to inelastic cross sections σ^{in} with values 1, 0.1, 0.05, 0.02, 0.01, 0.005, and 0.001 nm^2, respectively.

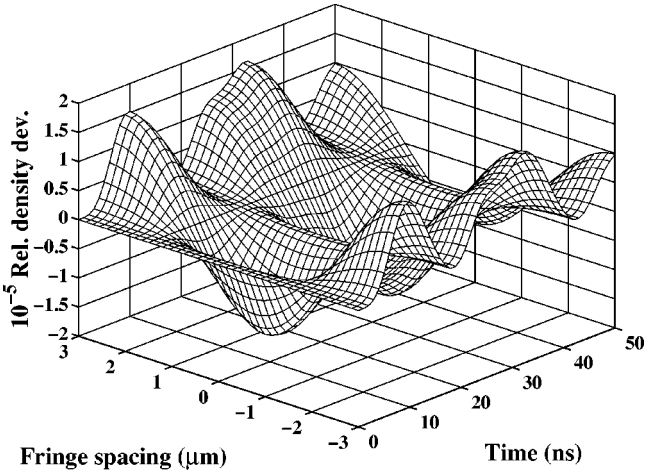

FIG. 15. Time-space evolution of the relative density deviation inside the fringe spacing for a Knudsen number Kn=1.67 and an inelastic cross section $\sigma^{in}=1$ nm^2.

Figures 6–11 show the results of DVM simulations for Knudsen numbers ranging from Kn=0.003 to 0.017 and inelastic cross sections from $\sigma^{in}=0.005$ to 1 nm^2. The gas mixture responds to the laser pulse with damped oscillations for both the number density and kinetic energy. The damping rate of the oscillations depends strongly on the Knudsen number, as can be seen in Figs. 8 and 9. For a Knudsen number Kn=0.003, the gas mixture oscillates more strongly and much longer than for Kn=0.017. The most significant difference in this context is that the general character of the density oscillations does not depend on the inelastic cross section, as can be seen in Fig. 10. In fact, the opposite is the case for the kinetic energy increase. For high values (strong quenching) the increase is accompanied by oscillations, whereas for low values the energy increases monotonously

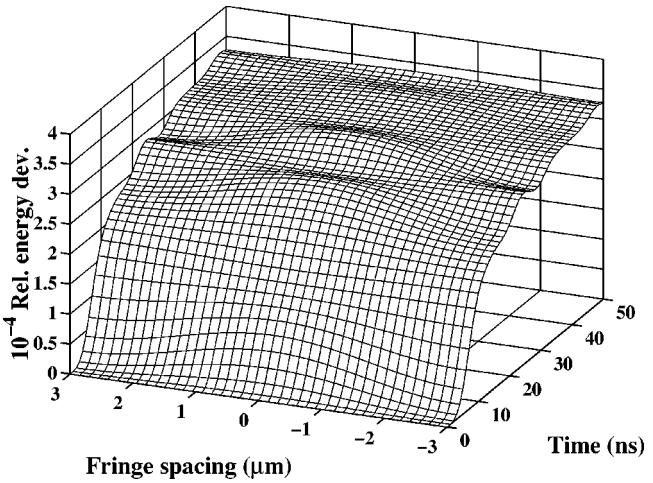

FIG. 16. Time-space evolution of the relative kinetic energy deviation inside the fringe spacing for a Knudsen number Kn=1.67 and an inelastic cross section $\sigma^{in}=1$ nm^2.

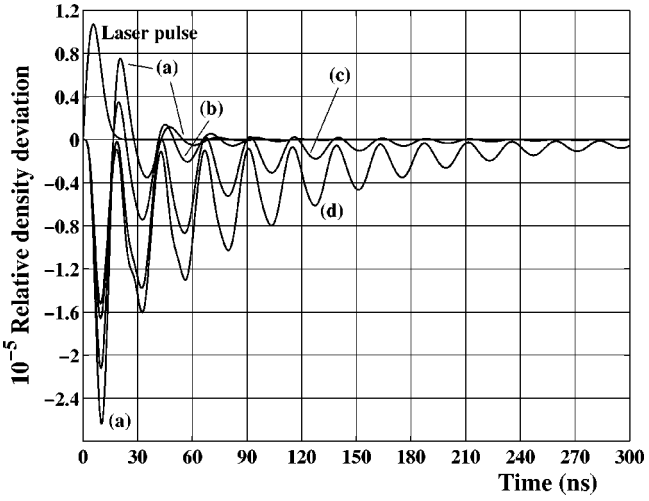

FIG. 17. Relative density deviation in the middle of the fringe spacing for an inelastic cross section $\sigma^{in}=1$ nm^2. (a), (b), (c), and (d) correspond to Knudsen numbers Kn with values 0.21, 0.33, 0.83, and 1.67, respectively.

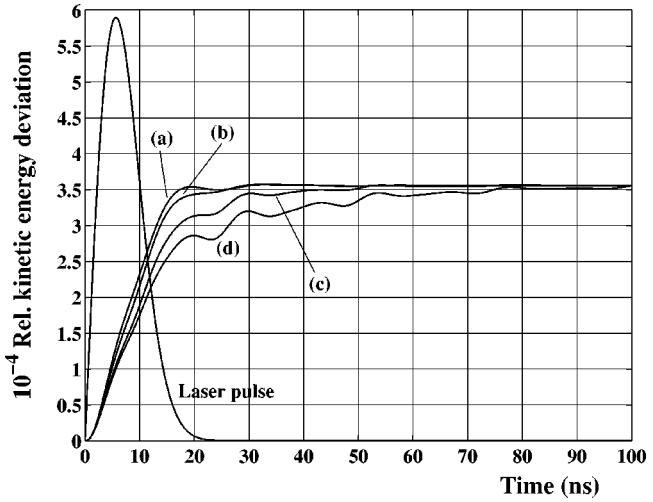

FIG. 18. Relative kinetic energy deviation in the middle of the fringe spacing for an inelastic cross section $\sigma^{in}=1$ nm^2. (a), (b), (c), and (d) correspond to Knudsen numbers Kn with values 0.21, 0.33, 0.83, and 1.67, respectively.

and spatially uniformly. This is demonstrated in Figs. 7 and Fig. 11.

B. Medium Knudsen numbers

In this range the equations of fluid dynamics lose gradually their validity. An interesting and unexpected behavior of the gas mixture exposes Fig. 12. The temporal density oscillations disappear almost completely with increasing Knudsen number. In other words, at Kn=0.083 the mechanisms controlling the damping effects reveal their strongest influence. Another demonstration that the inelastic cross section does not influence the general character of the oscillations is shown in Fig. 13. The strength of the oscillations decreases as the inelastic cross section decreases. Figure 14 shows the increase of the kinetic energy at Kn=0.083 for several inelastic cross sections. For low values of σ^{in} the deposition of the internal energy of the gas species A^* cannot take place rapidly, and, therefore, the kinetic energy of the whole gas mixture increases very smoothly.

C. High Knudsen numbers

This is the region where a molecular gas kinetic model has to be used. Figures 15–18 show the results of a simulation that a linearized hydrodynamical approach cannot provide. In Sec. III B, we observed that the density oscillations disappear until a Knudsen number Kn=0.083 is reached. However, the density oscillations regenerate with increasing Knudsen numbers, as demonstrated in Fig. 17. For Kn=1.67, the gas mixture is a Knudsen gas, which means that the gas behavior is mainly determined by the periodic boundary conditions. This explains the reappearance of the density oscillations. Moreover, the character of the oscillations gains more and more nonlinear features. Even the kinetic energy no longer increases monotonously, as can be seen in Figs. 17 and 18.

IV. CONCLUSION

This paper treats and simulates the physical processes behind the laser-induced thermal acoustics at a microscopic level. A regular discrete velocity model of Shizuta type with 36 velocities and six speeds proves capable of describing gas mixtures that interact with an intensity field of a laser. The model takes into account the most important interaction processes which dominate the physical behavior of the system. For low Knudsen numbers, the model provides the same results as obtained by numerically solving the equations of fluid dynamics in their linearized formulation. Our approach especially provides a description of the physics of four-wave mixing for higher Knudsen numbers. For medium Knudsen numbers it is shown that the oscillations are strongly damped and hardly appear. However, with increasing Knudsen number, the oscillations regenerate and show nonlinear temporal character. We attribute this phenomenon to almost free molecular flow of the gas particles through several fringe spacings. These consecutive fringe spacings give rise to the observed interference effects in this domain of rarefication.

ACKNOWLEDGMENTS

The present piece of research is part of a project supported by the Austrian Science Fund (FWF) through Contract No. P10879-TEC. One of the authors (W.K.) would like to express his gratitude toward the Rektor of the Technical University of Graz for financial support.

[1] S. Williams, L. A. Rahn, P. H. Paul, J. W. Forsman, and R. N. Zare, Opt. Lett. **19**, 1681 (1994).

[2] E. B. Cummings, Ph.D. thesis, California Institute of Technology, Pasadena, CA, 1995.

[3] A. C. Eckbreth, *Laser Diagnostics for Combustion Species and Temperature* (Abacus Press, Cambridge, MA, 1988).

[4] P. H. Paul, R. L. Farrow, and P. M. Danehy, J. Opt. Soc. Am. B **12**, 384 (1995).
[5] C. Cercignani, *The Boltzmann Equation and Its Applications*, Applied Mathematical Sciences Vol. 67 (Springer-Verlag, New York, 1988).
[6] C. Cercignani, *Mathematical Methods in Kinetic Theory*, *Applied Mathematical Sciences*, 2nd ed. (Plenum Press, New York, 1990).
[7] C. R. Garibotti and G. Spiga, J. Phys. A **27**, 2709 (1994).
[8] H. Cabannes (unpublished).
[9] R. Monaco and L. Preziosi, *Fluid Dynamic Application of the Discrete Boltzmann Equation* (World Scientific, Singapore, 1991).
[10] J. A. Broadwell, Phys. Fluids **7**, 1243 (1964).
[11] R. Gatignol, *Théorie Cinétique des Gaz à Répartition Discrète de Vitesses* (Springer-Verlag, Berlin, 1975), Vol. 36.
[12] H. Cabannes, J. Mec. **14**, 705 (1975).
[13] H. Cornille, Transp. Theory Stat. Phys. **26**, 359 (1997).
[14] J. Oxenius, *Kinetic Theory of Particles and Photons*, Springer Series on Electrophysics Vol. 20 (Springer-Verlag, Berlin, 1986).
[15] C. Reitshammer, F. Schürrer, and A. Rossani, Phys. Rev. E **58**, 3964 (1998).
[16] L. Lapidus and G. F. Pinder, *Numerical Solutions of Partial Differential Equations in Science and Engineering* (Wiley, New York, 1982).
[17] W. H. Press, W. T. Vetterling, S. A. Teukolsky, and B. P. Flannery, *Numerical Recipes in C The Art of Scientific Computing*, 2nd ed. (Cambridge University Press, Cambridge, 1992), Vol. 1.
[18] N. Bellomo, *Lecture Notes on the Mathematical Theory of the Boltzmann Equation*, Series on Advances in Mathematics for Applied Science Vol. 33 (World Scientific, Singapore, 1995).
[19] J. O. Hirschfelder, C. F. Curtiss, and R. B. Bird, *Molecular Theory of Gases and Liquids* (Wiley, New York, 1964).